Experiments in Fluids (2023) 64:128
https://doi.org/10.1007/s00348-023-03667-y

RESEARCH ARTICLE

Strength and timing of primary and secondary vortices generated by a rotating plate

Diego Francescangeli[1] · **Karen Mulleners**[1]

Received: 31 January 2023 / Revised: 31 March 2023 / Accepted: 8 June 2023 / Published online: 5 July 2023

Abstract

Accurate predictions of how vortices grow, evolve, and separate from aerodynamic objects are desirable for various applications ranging from autonomous aerial vehicles to wind turbines. Here, we present an experimental characterisation of the formation process of vortices created by the rotation of a thin rectangular flat plate. The plate is rapidly accelerated from rest up to a constant rotational velocity that was varied to explore the effect of the Reynolds number on the limit strength and the timing of successively generated vortices at the tip of the plate. The total non-dimensional positive circulation released at the tip of the plate during the entire rotation varies solely as a function of the angular position of the plate. Initially, all this circulation accumulates in a primary or starting vortex until this vortex separates after a constant non-dimensional time for all rotational velocities and different plate dimensions tested. An empirical model of the prediction of the limit strength of the primary vortex based on the constant non-dimensional formation is presented. The limit strength of the primary vortex is independent of the Reynolds number. After the primary vortex separates, a series of smaller secondary vortices form at the tip of the plate. These secondary vortices are discretely released at increasing time intervals. The timing of the release of the secondary vortices and their non-dimensional strength depend on the Reynolds number, and an empirical prediction model is presented.

1 Introduction

Large-scale vortex-dominated flows are ubiquitous in nature and engineering applications. For example, we think of bluff bodies wakes (Thompson et al. 2020), the wake of natural and robotic swimmers (Triantafyllou et al. 2000; Linden and Turner 2001; Dabiri 2009), leading-edge vortices on the wings of pitching, heaving, and flapping wings (Eldredge and Jones 2018), aerial vehicles encountering large gusts (Greenblatt and Williams 2021; Jones et al. 2021), etc. In such vortex-dominated flows, the forces experienced by the objects in the flow are mainly influenced by the circulatory forces created by the generation and shedding of vortices (Gehlert et al. 2023). Accurate prediction of the strength, time of separation, and trajectory of vortex forming on aerodynamic objects are desirable to create more accurate force prediction models.

When an object is accelerated from rest, vorticity is generated at the surface of the object (Morton 1984). If the object is an airfoil at a low angle of attack, the vorticity at the wall accumulates near the trailing edge and forms a primary or starting vortex in its wake (Luchini and Tognaccini 2002; Xu and Nitsche 2015; Sattari et al. 2012; Pullin and Perry 1980). If the angle of attack is high, vorticity can also accumulate near the leading edge and form a primary leading edge or stall vortex (Eldredge and Jones 2018; Muijres et al. 2008). A comparable scenario is observed when fluid is impulsively ejected through a circular nozzle or orifice. Here, vorticity accumulates in the shear layer between the fluid jet and the surrounding fluid, which rolls up into a primary vortex ring (Krueger and Gharib 2003; Shusser et al. 2002; Limbourg and Nedić 2021; Krueger 2008).

These primary or starting vortices do not grow indefinitely but reach a limit strength beyond which they will not take up additional circulation (Gharib et al. 1998; de Guyon and Mulleners 2021; Gao and Yu 2010; Mohseni and Gharib 1998). The vortex formation number is the non-dimensional time at which the primary vortex reaches its limit strength. Vortex formation numbers close to 4 are found in many natural and laboratory configurations. Onoue and Breuer

---

✉ Karen Mulleners
karen.mulleners@epfl.ch

[1] Institute of Mechanical Engineering, École polytechnique fédérale de Lausanne, Station 9, 1015 Lausanne, Vaud, Switzerland

(2016) found that the circulation of the leading edge vortex formed on a pitching plate reaches its maximum at a formation number of 3.7 ± 0.3. A similar value was also found by Ringuette et al. (2007), who observed the vortex pinch-off from an accelerating flat plate at a formation number of approximately 4. These values of the formation number are the same order of magnitude as those found by Gharib et al. (1998); Milano and Gharib (2005); Dabiri (2009) for a vortex ring ejected by a piston-cylinder apparatus. Limbourg and Nedić (2021) unified the formation number for orifice-generated vortex rings to values around 4 when adapting the non-dimensional time to account for the contraction of the flow.

Various studies also report different formation numbers. Dabiri and Gharib (2005) increased the formation number of the vortex ring by varying the nozzle exit diameter of a piston-cylinder apparatus in time. Shusser et al. (2006) increased the formation number by changing the piston velocity profile from a constant velocity profile to a profile with a constant acceleration. Krueger et al. (2006) reduced the formation number by putting the piston-cylinder apparatus in a uniform co-flow.

The vorticity released after the primary vortex has reached its limit strength will accumulate into smaller secondary vortices within a trailing shear layer. We refer to secondary vortices as the smaller coherent structures formed and shed after a larger primary or starting vortex. These secondary vortices are composed of the same signed vorticity as the primary vortex.

An essential difference between the primary and secondary vortices is their size and associated frequencies. Bloor (1964) observed that the ratio between the characteristic frequencies of primary and secondary vortices shed in the near-wake of cylinders varies with Reynolds number according to $f_K/f_{SL} = Re^{1/2}$, where f_K and f_{SL} are the shedding frequencies of the primary and secondary vortices. However, there is no consensus about the exponent value of the proposed relationship. Prasad and Williamson (1997) indicated that an exponent value of 0.67 works for Re up to 10^5 and Wei and Smith (1986) found 0.87 in the range from $Re = 1200$ to 11000. No clear relationships are established in the situation of an isolated primary vortex. Based on the flow visualisation around a submerged flat plate, Grift et al. (2019) identified shedding frequencies of secondary vortices in the range from 13 Hz to 20 Hz for different values of acceleration, velocity, and immersion depth. This range corresponds to a Strouhal number around 0.2, according to the plate geometry and kinematics used by the authors. The secondary vortex shedding frequency behind a vertical flat plate increases with an increasing acceleration of the flat plate (Rosi and Rival 2017).

We conducted experiments with a rotating rectangular flat plate to systematically study differences in the nature and the formation process of primary vortices and their secondary successors. We focused on the rotation motion because it is a basic but fundamental two-dimensional motion. Any two-dimensional motion can be decomposed into a pure rotation and a translation. An extensive body of literature can be found that discusses the vortex formation behind translating objects (de Guyon and Mulleners 2021; Fernando and Rival 2016; Rosi and Rival 2017; Paraz et al. 2016). The vortex formation process on a rotation object has received less attention.

For a range of maximal rotational velocities that lead to a Reynolds number ranging from 2500 to 12000, the typical flow development induced by the rotation from rest of a thin flat plate is characterised by the formation of a large primary or starting vortex followed by the discrete release of significantly smaller secondary vortices. In Francescangeli and Mulleners (2021), we described the trajectories of these vortices by a modified Kaden spiral. Here, we focus on the limit strength and timing of the separation of the primary and secondary vortices.

2 Experimental methods

Experiments have been conducted in an octagonal tank filled with water (Fig. 1a). The tank had an outer diameter of 0.75 m. In the centre of the tank, we placed a rectangular flat plate that was connected to a rotation mechanism. The attachment point was in the middle of the shorter side of the rectangle. The rotation mechanism rotated the plate around the central longitudinal axis for 180° in quiescent water at 21 °C.

We conducted a first series of measurements with a rectangular flat glass plate with length $l = 8\,\mathrm{cm}$, width or span $s = 16\,\mathrm{cm}$, and thickness $h = 2\,\mathrm{mm}$. The distance between the centre of rotation and the tip of the plate is referred to as the chord length c. We increased the thickness of the plate to $h = 4\,\mathrm{mm}$ for the second set of measurements. This second set allowed us to study the influence of the thickness on the formation of vortices. A third set of measurements included a plate with a longer length $l = 12\,\mathrm{cm}$, yielding a chord length of $c = 6\,\mathrm{cm}$. This third set provided insight into the influence of the chord length on the vortex formation.

The rotation mechanism was fastened to an outer aluminium frame such that the mid-span of the plate was in the centre of the tank to limit wall interference effects. A servo motor (Maxon RE 35) was connected to a stainless steel shaft, and the motion kinematics were transferred to the flat plate through a 1 : 1 conical coupling. A 1 : 19 gearbox was mounted on the motor to ensure high torque, speed, and acceleration. The rotational angle, speed, and acceleration were controlled via a motion controller (Galil DMC-40), which allowed for accurate control of arbitrary

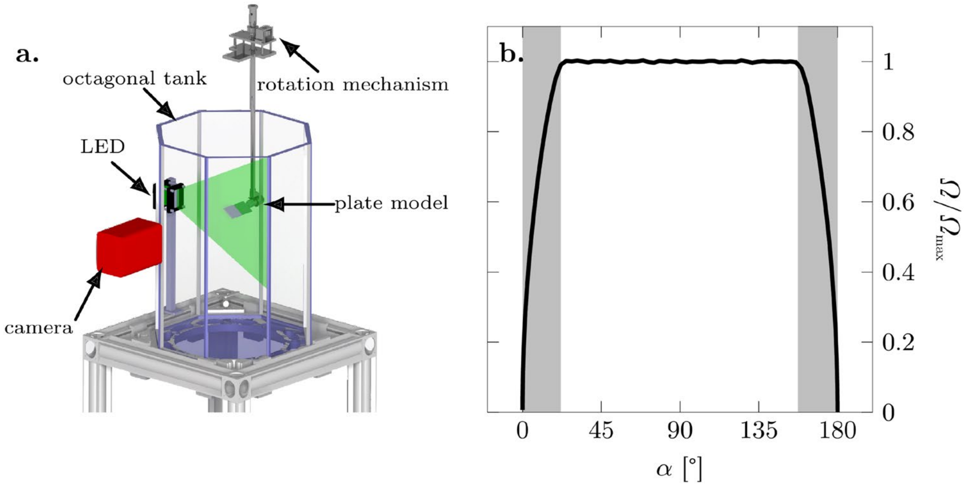

Fig. 1 **a** Schematic of the experimental set-up and the rotation mechanism. **b** Trapezoidal velocity profile as a function of the angular position. The grey shaded regions indicate the portion of the motion during which the plate is accelerated

motion profiles. The rotation programme was a trapezoidal rotational velocity profile with a fixed rotational amplitude of 180° (Fig. 1b). The error between the motor input signal and the motor response measured by the encoder remained below 0.1° throughout the entire motion for all parameter variations considered.

To ensure a continuous acceleration profile, the corners of the velocity trapezoid were smoothed. The maximum rotational speed Ω_{max} was varied from 100 °/s to 400 °/s. This led to a Reynolds number $Re = (\Omega_{\max} c^2)/\nu$ ranging from 2790 to 11150. Here, ν is the kinematic viscosity of the water and the chord c is defined as the distance between the centre of rotation and the tip of the plate. The rotational acceleration $\dot{\Omega}$ was fixed at $6000°/\mathrm{s}^2$.

The velocity field in the cross-sectional plane at the model mid-span was measured using planar particle image velocimetry (PIV). A high-power pulsed light-emitting diode (LED Pulsed System, ILA_5150 GmbH) was used to create a light sheet that forms the measurement plane. The applicability of high-power LED for PIV has been demonstrated previously by Willert et al. (2010); Krishna et al. (2018). Time-resolved PIV images were recorded with a Photron FASTCAM SA-X2 high-speed camera. The camera was equipped with a 35 mm lens (Canon EF f/2 IS USM), and the camera was aligned carefully such that the optical axis of the lens was aligned with the rotational axis of the plate and perpendicular to the light sheet (Fig. 1a). The frame rate and the exposure time were varied depending on the maximum rotational speed. A frame rate and exposure time of 250 Hz and 1 ms were selected for a rotational speed of 30°/s. They were adapted to 2000 Hz and 0.5 ms for the highest tested speeds. Each case was repeated 5 or 6 times. The frame rate of the camera was high enough to capture the dynamics of the motion, and the LED was set to continuous mode. The camera resolution was 1024 px × 1024 px, which corresponded to a field of view of 20 cm × 20 cm.

The raw data were processed by the commercial software PIVview (PIVTEC GmbH, ILA 5150 GmbH) using a correlation model based on minimum squared differences and a multi-grid interrogation algorithm with three iterations. The final interrogation window size was 32 px × 32 px with an overlap of 68%. A third-order B-spline interpolation method for sub-pixel image shifting was performed on all passes. The resulting physical resolution was 1 mm, or 0.025c with $c = 4\,\mathrm{cm}$.

The total displacement error for PIV data is the sum of a random error or measurement uncertainty and a bias error. We measured an average particle displacement of 4 px between two subsequent frames, which led to a global random error of 0.175 px or 4.3% according to Raffel et al. (2018); Nobach and Bodenschatz (2009). The bias error is mainly determined by peak locking, a phenomenon describing the tendency of the displacements to be biased toward integer pixel values. Histograms of subpixel displacement showed that peak locking was successfully avoided, and the remaining bias error was assumed to be significantly less than the random error (< 0.05 px).

3 Results

The typical flow topology that we observe when we rotate a rectangular plate with a chord-based Reynolds number ranging from 2790 to 11170 is presented in Fig. 2a-c. The formation of a large primary vortex is followed by the occurrence of smaller secondary vortices that move along a spiralling trajectory. The secondary vortices are discretely released from the plate tip, and we refer to this tested range of Reynolds number as the discrete shedding regime (Francescangeli and Mulleners 2021).

The timing of the discrete shedding of the individual secondary vortices is estimated using the swirling strength

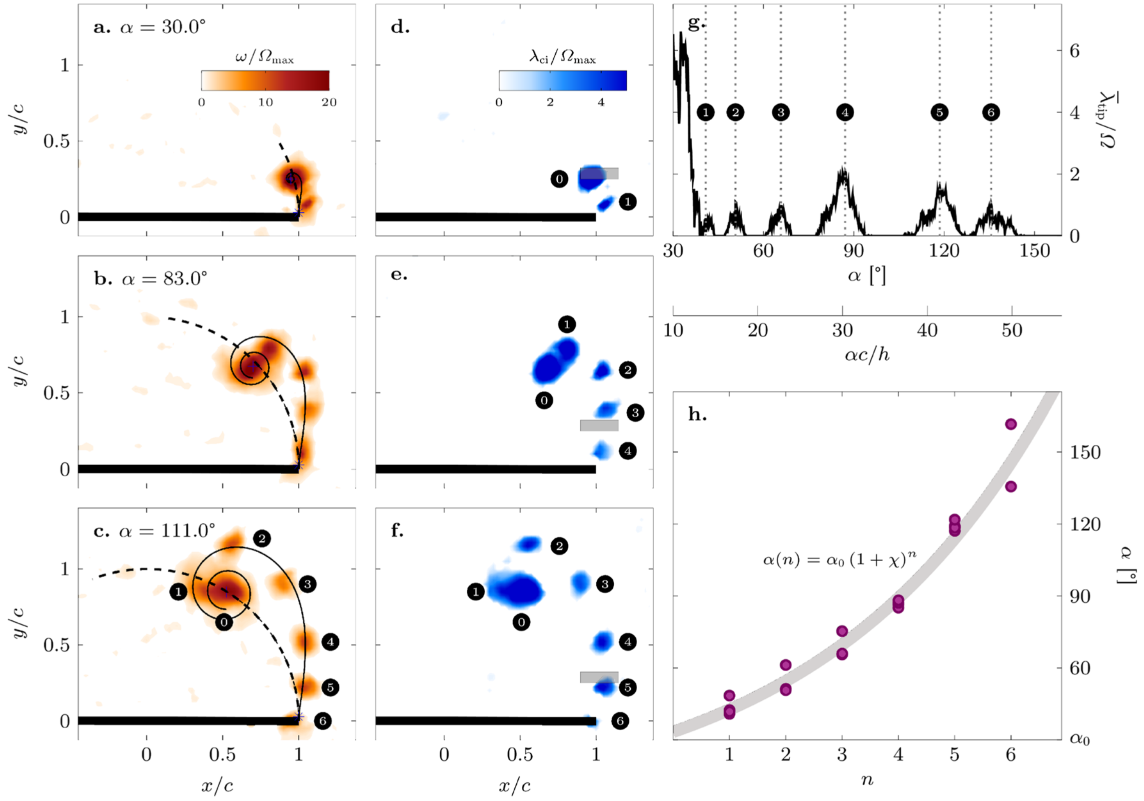

Fig. 2 Temporal evolution of vorticity and swirling strength λ_{ci} at the angular position (**a**, **d**) $\alpha = 30.0°$, (**b, e**) $\alpha = 83.0°$ and (**c**, **f**) $\alpha = 111.0°$. The black curve is the modified Kaden's spiral defined in Francescangeli and Mulleners (2021). The dashed line represents the plate tip trajectory. The grey rectangles in **d**–**f** indicate the probing area for the local average swirling strength. **g** Evolution of $\overline{\lambda}_{tip}$ as a function of the angular position of the plate. The dotted lines mark the separation angle of subsequent secondary vortices. **h** Delay between the successive shedding of secondary vortices as a function of the shedding order n for $Re = 8380$. The solid line is the power law fit

criterion introduced by Zhou et al. (1999). A vortex is considered a connected region when the value of the swirling strength λ_{ci} is positive (Fig. 2d-f). The evolution of the local average swirling strength, denoted by $\overline{\lambda}_{tip}$, in a small rectangular probing area close to the tip of the plate for $Re = 8380$ is presented in Fig. 2g. The probing area is indicated in Fig. 2d-f by the grey rectangle centred around $x/c = 1.02$ and $y/c = 0.29$. The location and size of the average tip swirling strength probing region were selected after a sensitivity analysis (Francescangeli and Mulleners 2021).

The temporal evolution of $\overline{\lambda}_{tip}$ has a global maximum and first peak, followed by six clearly distinguishable smaller peaks. The initial peak corresponds to the passage of the primary vortex through the probing area, and the subsequent smaller peaks mark the shedding of individual secondary vortices. The local maxima of the six smaller peaks is used to mark the shedding timing of the secondary vortices and can be expressed in terms of α or in terms of the non-dimensional convective time $\alpha c/h$.

The timing of the shedding of subsequent secondary vortices for $Re = 8380$ in terms of α is presented in Fig. 2h. Different markers with the same vortex number correspond to multiple repetitions of the experiment. Secondary vortices are not released at constant intervals during the rotation. The timing between subsequently released vortices increases the more secondary vortices have been previously released. As shown at the end of our previous paper (Francescangeli and Mulleners 2021), the timing can be described by a power law:

$$\alpha(n) = \alpha_0(1+\chi)^n \quad , \tag{1}$$

where $\alpha(n)$ indicates the angular position at the shedding of the n-th secondary vortex and α_0 and χ are fitting parameters. The timing dynamics for all Reynolds numbers in the discrete shedding regime can be represented by the power law given by Eq. (1). The fitting parameters α_0 and χ are presented in Fig. 3 as a function of the Reynolds number. The influence of the location and size of the probing region on the fitting parameter is minor and is discussed in appendix A. The data presented in Fig. 3 is also provided in form of a table in appendix B.

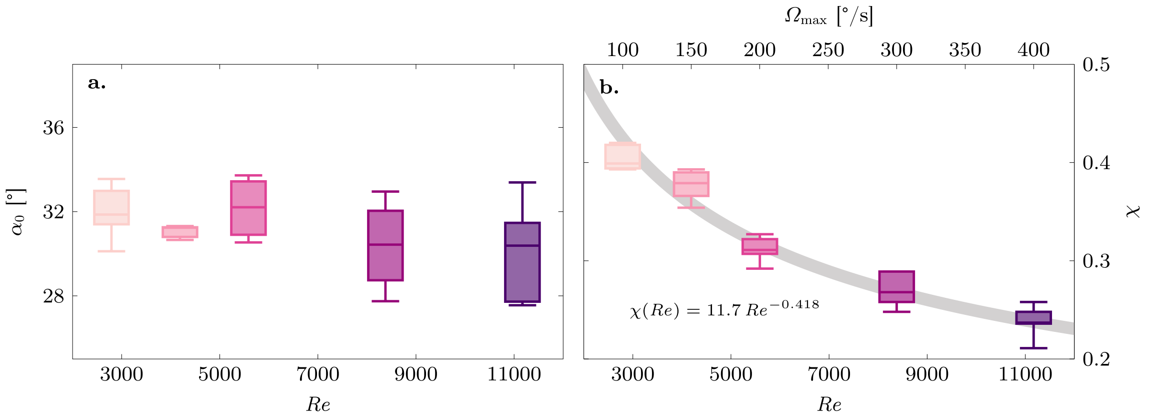

Fig. 3 Fitting parameters **a** α_0 and b χ as a function of the Reynolds number. The solid grey line in **b** is the power law fit given in Eq. (2). The data presented here is also provided in form of a table in table 1

The mean value of α_0 across different experiments does not vary significantly with the Reynolds number and we find an average value of $\alpha_0 = (31 \pm 2)^\circ$ for all rotational motions using the plate with $h = 2$ mm and $c = 4$ cm (Fig. 3a). Based on Eq. (1), α_0 corresponds to the angular position at which $n = 0$. We will confirm in the next section that this corresponds indeed to the location at which the primary vortex separates.

The value of χ strongly depends on the Reynolds number and decreases when the plate rotates faster (Fig. 3b). The decrease of χ with Reynolds number can again be described by a power law

$$\chi = aRe^{-b}, \tag{2}$$

with a and b fitting parameters. For the tested range of Reynolds numbers from 2500 to 12000, we find $a = 11.7$ and $b = 0.418$ for the best fit indicated by the solid grey line in Fig. 3. By rearranging Eq. (1), we can write:

$$\chi = \frac{\alpha(n+1)}{\alpha(n)} - 1 \tag{3}$$

Lower values of χ thus indicate a faster succession of secondary vortices and the shedding of more secondary vortices over a constant 180 ° rotation.

3.1 Primary vortex growth and separation

Here, we focus on the growth and subsequent separation of the primary vortex from the rotating plate. As a first step, we want to verify that the value of α_0 found as the result of fitting Eq. (1) to the experimental data indeed corresponds to the location at which the primary vortex separates from the feeding shear layer. To do so, we concentrate on the evolution of the flow topology for rotational angles around $\alpha = \alpha_0$. For a Reynolds number of 8380, we find $\alpha_0 \approx 30.4^\circ$ (Fig. 2h). Positive (pFTLE) and negative finite-time Lyapunov exponent (nFTLE) fields (Haller 2001, 2015) have been calculated for rotational angles below and above α_0 and the ridges in the FTLE fields are presented in Fig. 4. The ridges help identify the boundaries of coherent structures and the intersections between the ridges of the positive and negative FTLE fields mark the location of a saddle point. The emergence of saddles points indicate vortex detachment (Mulleners and Raffel 2012; Huang and Green 2015; Rockwood et al. 2017; Krishna et al. 2018). The saddle point closest to the wing tip is highlighted by circles in Fig. 4. When the plate is at an angular position $\alpha < \alpha_0$, the negative ridges are not yet well-formed (Fig. 4a). At this stage, no clear intersections between positive and negative FTLE ridges that mark the location of a saddle point are detected. This suggests that the feeding process of the primary vortex is still in progress. At $\alpha = 33^\circ$, the negative ridges are now clearly delineated (Fig. 4b). An intersection between the negative and the positive FTLE ridges emerges close to the tip of the plate and is located along the shear layer that feeds the primary vortex (Fig. 4b). When the plate rotates beyond α_0, the distance between the saddle point and the tip increases as the saddle point moves away together with the primary vortex (Fig. 4c).

The emergence of the saddle point near α_0 represents the instant at which the primary vortex pinches-off from the plate tip. When the primary vortex separates from the feeding shear layer, the vortex circulation stops increasing. To measure the primary vortex circulation, we first need to identify its boundaries. We use both the swirling strength λ_{ci} criterion and the dimensionless Galilean invariant scalar function Γ_2 (Graftieaux et al. 2001) to identify the boundaries of the primary vortex. The primary vortex circulation is obtained by integrating the positive vorticity inside the selected boundary contour. The influence of the different vortex boundary identification criteria on the measure of the vortex circulation is discussed in appendix C.

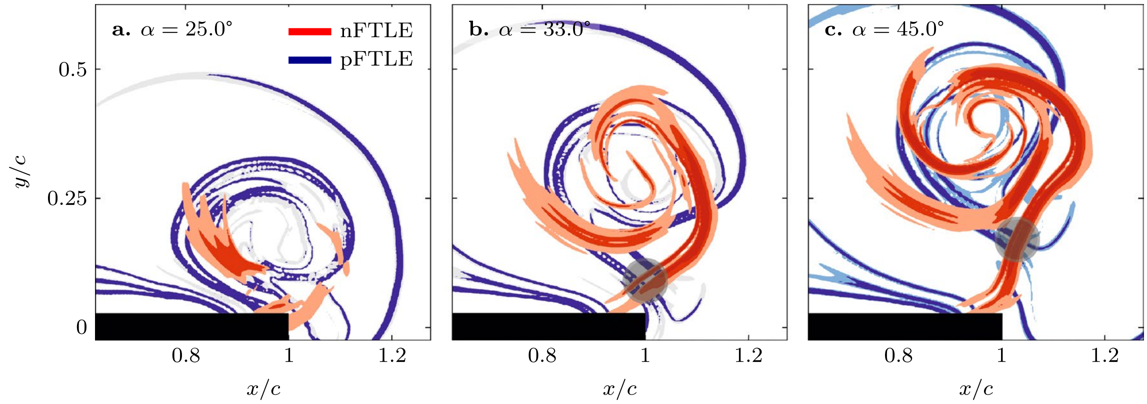

Fig. 4 Positive and negative FTLE ridges at **a** $\alpha < \alpha_0$, **b** $\alpha \approx \alpha_0$ and **c** $\alpha > \alpha_0$ for $Re = 8380$. The black circle highlights the location of the saddle point

The temporal evolution of the primary vortex circulation is presented by markers in Fig. 5 for $Re = 4190$ and $Re = 8380$. The solid lines in Fig. 5 indicate the evolution of the total circulation obtained by integrating all positive vorticity released from one side of the plate. The bottom x-axis indicates the rotational angle of the plate, which corresponds to the ratio between the travelled arc length $l(t) = \Omega(t)\,t\,c = \alpha(t)c$ and the chord length c. The chord of the plate is defined as the distance between the point of rotation and the plate tip. An alternative convective time measure can be calculated as the ratio between the travelled arc length $l(t) = \Omega(t)\,t\,c$ and the thickness of the plate h, which is indicated by the top x-axis.

The total circulation associated with the positive vorticity released on one end of the plate continuously increases in time. The rate of increase changes during the rotation and is higher at the beginning of the motion. The rotational acceleration for our measurements is kept constant at $6000°/\mathrm{s}^2$, which leads to increasing acceleration times for increasing maximum rotational speeds. For the largest rotational speed tested, the acceleration phase ends at $\alpha = 24°$, which is still well before the primary vortex separates at α_0.

When the plate starts rotating, all positive vorticity accumulates in the primary vortex and the primary vortex circulation Γ_0, indicated by the markers, matches the total circulation Γ_{tot} (Fig. 5). When the plate has travelled approximately 31°, the primary vortex circulation ceases to increase while the total circulation keeps increasing. The angular position at which the primary vortex circulation reaches its maximum value coincides with the emergence of a saddle point in the flow field (Fig. 4b) and matches the value indicated by the fitting parameter α_0.

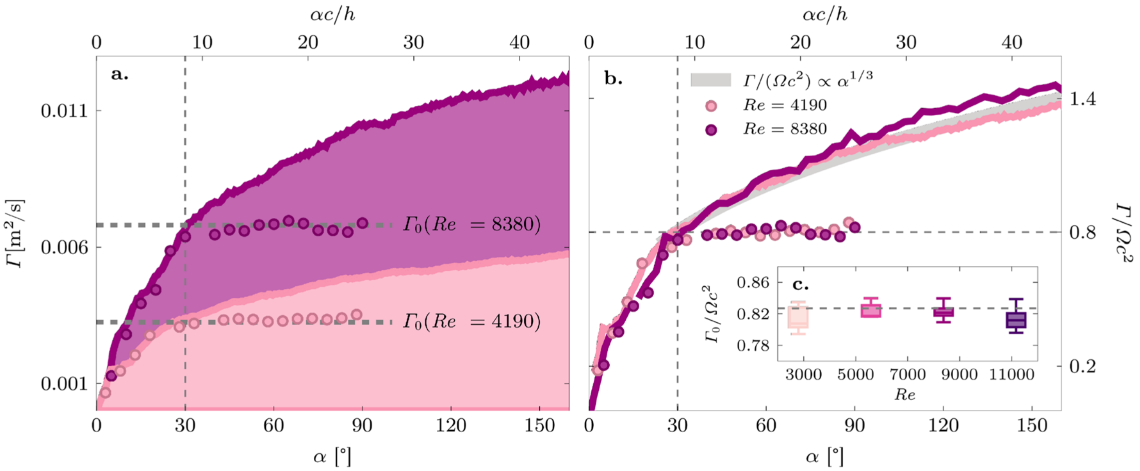

Fig. 5 Temporal evolution of the **a** dimensional and **b** dimensionless primary vortex and total circulation for $Re = 4190$ and $Re = 8380$. The solid grey line in **b** indicates the theoretical temporal evolution of $\Gamma/(\Omega c^2)$ as predicted by inviscid theory. **c** Non-dimensional circulation of the primary vortex, $\Gamma_0/(\Omega c^2)$, measured at $\alpha = \alpha_0$, as a function of the Reynolds number. The dashed line in **c** is the prediction of the maximum primary vortex circulation following Eq. (6)

When the vortex pinches-off, circulation is no longer entrained in the primary vortex and the additional circulation accumulates in the form of secondary vortices that will be discretely released during the rest of the motion. The overall growth of the circulation and final dimensional value of the primary vortex circulation increases with increasing Reynolds number. We measure final values of $\Gamma_0 = 0.0032 \pm 0.0001\,\mathrm{m^2/s}$ and $\Gamma_0 = 0.0062 \pm 0.0002\,\mathrm{m^2/s}$ for $Re = 4190$ and $Re = 8380$, respectively (Fig. 5a). The evolution of the non-dimensional circulation, expressed as $\Gamma(t)/(\Omega(t)c^2)$, is independent of the Reynolds number (Fig. 5b). Across the Reynolds number range tested, we find a constant maximum non-dimensional primary vortex strength of $\Gamma_0/(\Omega c^2) = 0.81 \pm 0.02$ for all rotational motions using the plate with $h = 2\,\mathrm{mm}$ and $c = 4\,\mathrm{cm}$ (Fig. 5c).

The initial growth in circulation reduces once the primary vortex has separated. For $\alpha \geq \alpha_0$, the increase in the total non-dimensional circulation is described by

$$\Gamma/(\Omega c^2) = K\alpha^{\frac{1}{3}}, \tag{4}$$

where the fitting constant $K = 1.0$ for our experimental data if α is expressed in radians. The fit is shown by the thick grey line in Fig. 5b. The increase in the dimensionless total circulation with $\alpha^{1/3}$ is similar to the behaviour observed by Pullin et al. for a two-dimensional plate moving at a constant speed (Pullin 1979; Pullin and Wang 2004; Pullin and Sader 2021). This result is also experimentally and numerically confirmed by Rival et al. (2014) and Xu and Nitsche (2015).

Pullin (1978) derived the temporal evolution of the total circulation shed by a translating wedge that is started from rest by assuming a potential flow and a power law translation profile given by $U(t) = U_0\hat{T}^m$, with U_0 a velocity constant and $\hat{T}$ the non-dimensional time. By considering a zero wedge angle and a constant velocity, the expression for the total dimensionless circulation derived by Pullin (1978) simplifies to:

$$\hat{\Gamma}(t) = \mathcal{J}\hat{T}^{1/3} \tag{5}$$

for a vertical flat plat that is impulsively translated horizontally from rest. Here, $\hat{\Gamma}$ and $\hat{T}$ are the dimensionless circulation and time based on U_0, and $\mathcal{J}$ is the dimensionless shed circulation constant. The shed circulation constant $\mathcal{J}$ depends on the wedge angle and the power coefficient m of the velocity profile. For a flat plat that is impulsively started from rest to a constant velocity U_0, Pullin found $\mathcal{J} = 2.4$. Recently, Pullin and Sader (2021) extended the prediction of the circulation of the starting vortex for flat plates subjected to a translating start-up motion coupled to a plate rotation. They show how the shed circulation constant varies with the rotational-to-translational velocity ratio. Unfortunately, no solution for a purely rotational motion is available and no direct comparison with our experimentally determined value can be made. The spatial velocity gradient experienced at the tip of the plate due a rotational motion differs from the gradient experienced when the plate is translated, which would yield different shed circulation constants. Yet, the temporal evolution of the circulation is governed by the same power law coefficient in both cases.

For $\alpha \geq \alpha_0$, the evolution of the total circulation is governed by Eq. (4) and the maximum circulation of the primary vortex equals the total circulation at $\alpha = \alpha_0$. The limit strength of the primary vortex can thus be estimated by:

$$\Gamma_0/(\Omega c^2) = K\alpha_0^{\frac{1}{3}}, \tag{6}$$

with $K = 1.0$ and $\alpha_0 = 31 \pm 2°$ the empirically determined values for the Reynolds numbers ranging from 2790 to 11170 that were tested here (Fig. 5c).

3.2 Primary vortex formation number and analogy with translational vortex ring generation

When a volume of fluid is ejected through a circular nozzle in otherwise quiescent fluid, a vortex sheet is created at the outlet of the nozzle. This vortex sheet rolls up into a coherent primary or starting vortex ring (Pullin 1979; Glezer 1988; Shariff and Leonard 1992). The vortex ring will not grow indefinitely and a few convective times after the vortex sheet is created, the self-induced velocity of the vortex ring exceeds the velocity of the shear layer that feeds it, and the vortex pinches off (Shusser and Gharib 2000). After the vortex pinches off, its circulation ceases to increase and its non-dimensional energy reaches a characteristic minimum value that depends on the velocity distribution in the ejected fluid (Gharib et al. 1998; Mohseni et al. 2001; Limbourg and Nedić 2021). The convective time at which these propulsive vortex rings simultaneously pinch off, reach a minimal non-dimensional energy, and outpace their feeding shear layer is referred to as the vortex formation number (Gharib et al. 1998; Mohseni and Gharib 1998).

A commonly used approach to estimate the vortex formation number for piston-generated vortices is the asymptotic matching procedure (Limbourg and Nedic 2021b). In this procedure, values of the circulation, impulse, and energy of the fluid ejected by the piston are predicted by a slug-flow model (Mohseni and Gharib 1998; Shusser et al. 1999; Linden and Turner 2001). The formation number is identified as the formation time at which the estimated invariants match the equivalent asymptotic values for an isolated vortex ring that corresponds to a certain family of vortex rings. The vortex ring invariants can be combined to estimate the translational velocity of a vortex ring (Saffman 1975) and the asymptotic matching procedure can be formulated as a kinematic argument for vortex pinch-off.

The formation number is then identified as the formation time at which the translational velocity of the vortex exceeds the shear layer velocity. This approach requires an accurate estimation of the shear layer velocity. A rough approximation is to consider the shear layer velocity to be half of the piston velocity (Mohseni and Gharib 1998). More accurate approximations use the spatial velocity profile at the nozzle exit or take the contraction ratio of the starting jet into account (Weigand and Gharib 1997; Limbourg and Nedic 2021a).

For vortices that form in the wake of translating or rotating bodies, the self-induced velocity of the vortex cannot be estimated based on the slug-flow model as the volume and the velocity of the fluid injected in the vortices are not known a priori. Here, we can use the approach proposed by de Guyon and Mulleners (2022) that is based on the self-similar vortex sheet roll-up or directly measure the velocity of the vortex centre. We chose the later option.

The primary vortex that forms due to the rotation of our flat plate moves on a circular trajectory following the plate's tip, indicated by the dotted line in Fig. 6a (Francescangeli and Mulleners 2021). The angular position of the primary vortex core with respect to the plate is indicated by β. The temporal evolution of β is solely determined by the plate's rotational angle α and does not vary with the Reynolds number for a given plate geometry (Fig. 6b). The relative speed of the primary vortex U_0 with respect to the plate is given by

$$\mathrm{U}_0(t) = \frac{\mathrm{d}(\beta c)}{\mathrm{d}t} = c\frac{\mathrm{d}\beta}{\mathrm{d}\alpha}\frac{\mathrm{d}\alpha}{\mathrm{d}t} = \Omega(t)c\frac{\mathrm{d}\beta}{\mathrm{d}\alpha} \quad . \tag{7}$$

To facilitate calculations, we approximate the variation of β with α by a second order polynomial.

The evolution of the calculated primary vortex speed U_0 normalised by the maximum plate's tip speed $\mathrm{U}_{tip} = \Omega_{max}c$ is presented in Fig. 6c for different Reynolds numbers. During the acceleration of the rotational motion, the curves corresponding to the different Reynolds numbers are separated because the vortex speed is normalised by the maximum tip speed. The different Reynolds numbers correspond to rotational motions with different maximum rotational velocities with the same rotational acceleration, which leads to larger durations of the acceleration phase for the higher Reynolds number cases. After the acceleration phase, the $\mathrm{U}_0/\mathrm{U}_{tip}$ curves of the different cases collapse as β depends solely on α for a given plate geometry. When the primary vortex separates around α_0, the primary vortex centre follows the tip with a velocity that is slightly higher than half of the plate tip's velocity which matches the conditions of vortex separation for piston-generated vortices (Mohseni and Gharib 1998).

To determine a vortex formation number for the primary vortex by analogy with piston-generated vortices, we need to select the non-dimensional convective timescale that is most suitable to describe the vortex formation process. The two most obvious choices for non-dimensionalising time are defining the convective time as the ratio between the arc length travelled by the plate tip and the chord length which is α; or as the ratio between the arc length travelled by the plate tip and the thickness of the plate which is $\alpha c/h$. To determine which scaling is more appropriate to characterise the age of the primary vortex generated by the rotating plate, we now consider results for different plate geometries.

Figure 7 summarises the temporal evolution of the total circulation (Fig. 7a) and the primary vortex circulation as a function of the chord-based convective time (Fig. 7b) and the thickness-based convective time (Fig. 7c) for three plates with 2 cm or 4 mm thickness and 4 cm or 6 cm chord length

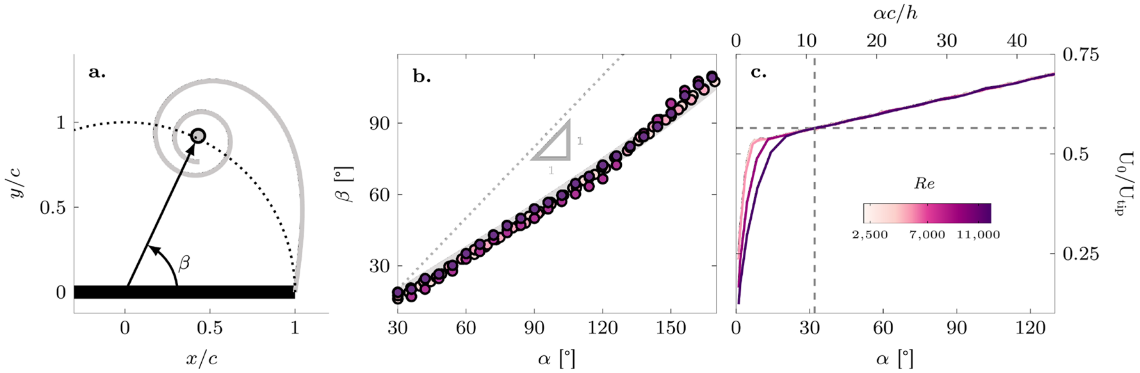

Fig. 6 **a** Definition of the angle β indicating the angular position of the primary vortex with respect to the plate. **b** Evolution of β as a function of the plate's rotation angle α for different *Re*. **c** Normalised speed of the primary vortex centre as a function of the plate's rotation angle for different *Re*. The vertical dashed line in **c** indicates the angle α_0 at which the primary vortex separates. The horizontal dashed line in **c** indicates the normalised vortex speed at separation

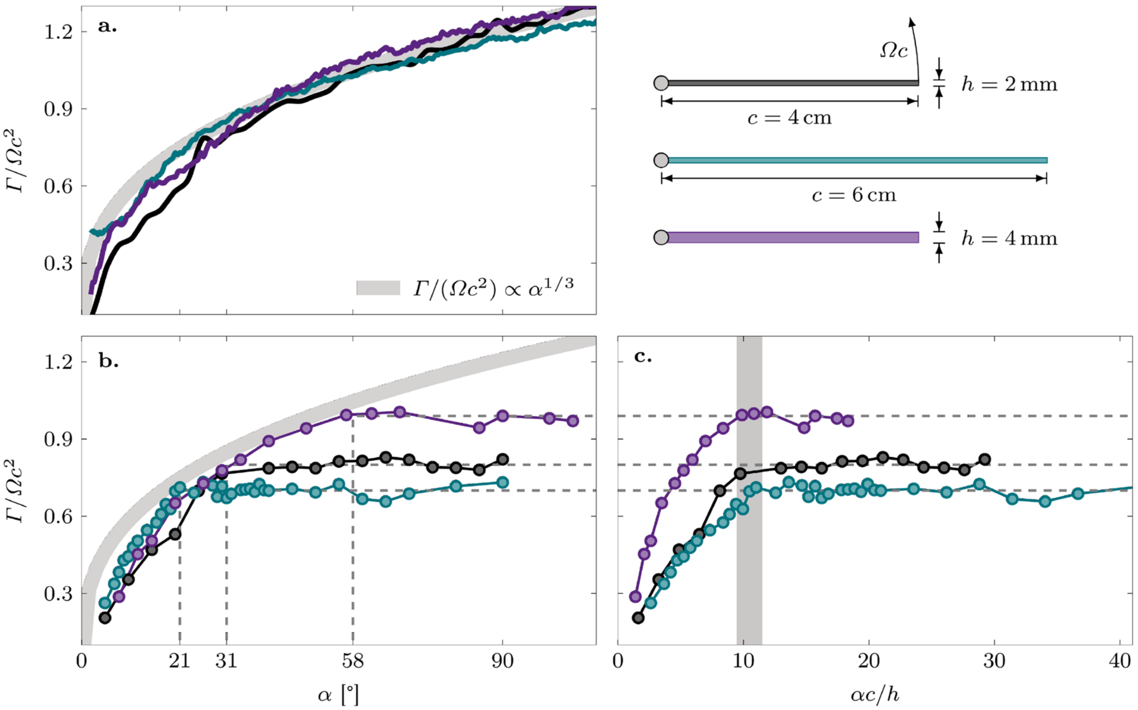

Fig. 7 Comparison of the evolution of the circulation of the rotation of three different plate geometries at Re =8380. **a** Evolution of the total circulation as a function of the plate's angle of rotation. **b** Primary vortex circulation as a function of α and **c** as a function of $\alpha c/h$

at $Re = 8380$. The total circulation for all three plates is governed by the plate's rotation angle and follows the inviscid theoretical prediction where $\Gamma/(\Omega c^2) \propto \alpha^{1/3}$. Deviations from the theoretical curve occur during the acceleration phase of the plate.

Initially, all circulation accumulates into the primary vortex and the primary vortex circulation closely matches the total circulation when presented as a function of α (Fig. 7b). Small discrepancies are due to the identification of the primary vortex boundaries. For our reference plate with a chord length of 4 cm and a thickness of 2 mm, the vortex separates around $\alpha = 31°$ and reaches a maximum non-dimensional circulation of $\Gamma_0/(\Omega c^2) = 0.81 \pm 0.02$. When the chord of the plate is increased from 4 cm to 6 cm for a constant thickness, the primary vortex circulation ceases to increases earlier at $\alpha \approx 21°$ and reaches a lower final value of $\Gamma_0/(\Omega c^2) \approx 0.7$. When we increase the thickness of the plate from 2 mm to 4 mm for a constant chord length, the primary vortex circulation continues to increase longer until $\alpha \approx 58°$ and reaches a higher final value of $\Gamma_0/(\Omega c^2) \approx 1.0$. The final value of the primary vortex is given by the angle at which the vortex separates, which is not constant for the different plate geometries. The convective time defined using Ωc as the characteristic velocity and c as the characteristic length scale thus provides a measure for the vortex strength but is not suitable to predict the primary vortex saturation and separation.

In Fig. 7c, we present the evolution of the primary vortex circulation for the three plates as a function of the convective time $\alpha c/h$. Now, the convective time at which the primary vortex circulation ceases to increase for all plate geometries occurs at the same non-dimensional time and yield a constant vortex formation number of $\alpha c/h = 10.9 \pm 0.6$. The convective time defined using Ωc as the characteristic velocity and h as the characteristic length scale provides a measure for the age of the primary vortex or how far it is away from saturation and separation and is suitable to define a vortex formation number.

The thickness and the chord length have a different effect on the vortex formation process that we try to explain here by analysing its effect on the vorticity distribution in the vortex. Vorticity is generated at the surface of the plate and predominantly at the plate tip where the velocity is highest. The vorticity then spreads across the shear layer at the tip that has a thickness that scales with the thickness of the plate. The shear layer rolls-up into the primary vortex and the tightness of this roll-up is governed by the chord of the plate. The tightness of the roll-up refers to the degree of compactness of the spiral created by the shear layer roll up. A tighter roll-up leads to a smaller and more compact spiral with less variation in the local curvature between successive windings, which leads to a more uniform distribution of vorticity in the core. The thicker the shear layer and tighter the roll-up, the more uniform the vorticity distribution in the core of the vortex, which is quantified by its non-dimensional energy (Saffman 1975; Weigand and Gharib 1997; de Guyon and Mulleners 2021). More uniform distributions of vorticity are characterised by lower values of the minimum non-dimensional energy, and higher non-dimensional circulation (Shusser et al. 1999; Mohseni et al. 2001; de Guyon and Mulleners 2022). Therefore, the vortex created by the thicker plate with the shorter chord is expected to have the lowest non-dimensional energy and highest circulation. The thinner plate with the longer chord has a higher concentration of vorticity in the shear layer which rolls up in a less tight spiral creating a vortex with a higher gradient of vorticity in the core, higher non-dimensional energy, and lower circulation.

Based on our experimentally determined constant formation number of $\alpha c/h = 10.9 \pm 0.6$ and the relationship between the primary vortex strength and the angle of the plate at separation given by Eq. (6), we can estimate the primary vortex strength for a large range of rotating flat plates by

$$\Gamma_0/(\Omega c^2) = 2.22\,(h/c)^{1/3}. \tag{8}$$

For the three plates tested this gives us $\Gamma_0/(\Omega c^2) = 0.71$, 0.82, and 1.0, which are indicated by the horizontal dashed lines in Fig. 7.

3.3 Secondary vortex strength

This section is dedicated to the circulation of the secondary vortices. The circulation of the secondary vortices is indicated by Γ_n, with n referring to the order in which they have shed. The circulation is calculated following the same procedure used for the primary vortex which relies on the swirling strength criterion to determine the vortex boundary. Fig. 8a represents the evolution of Γ_n as a function of the shedding order n for the plate with a chord length of 4 cm and a thickness of 2 mm at Re = 5589. The secondary vortices have median circulation values that range from 0.07 to 0.12, which makes them smaller than 20% of the primary vortex. Contrarily to what we hypothesised in Francescangeli and Mulleners (2021), the strength of the subsequent secondary vortices is not constant, but increases in time whereas the timing between the subsequent shedding of secondary vortices decreases.

Again, we can attempt a phenomenological explanation based on changes in the vorticity distribution in the shear layer. The strength of the shear layer at the tip of the plate is related to the velocity difference across the shear layer (Rosi and Rival 2017). When the plate is rotating at the constant rotational velocity, the temporal variation of the velocity difference across the shear layer is only influenced by the induced velocity due to the previously shed vorticity (Gehlert and Babinsky 2021; Gehlert et al. 2023). In time, the shed vorticity increases and the induced velocity decreases the strength of the shear layer, which also leads to a decrease in time in the total rate of increase of the circulation ($\dot{\Gamma} \propto 1/3\alpha^{-2/3}$). If we assume that the thickness of the shear layer scales with the thickness of the plate, then a decreases in the shear layer strength leads to a more uniform vorticity distribution, which are characterised by lower minimum values of the non-dimensional energy, and higher non-dimensional circulation of the individually shed vortices (Pullin 1978; de Guyon and Mulleners 2022). For all Reynolds numbers, we indeed observe an increase of the non-dimensional circulation of the subsequently shed vortices (Fig. 8b). The primary vortex has a constant non-dimensional maximum circulation for this range of Reynolds numbers (Fig. 5c), but the circulation of the secondary vortices decreases with increasing rotational velocity based Reynolds number (Fig. 8b).

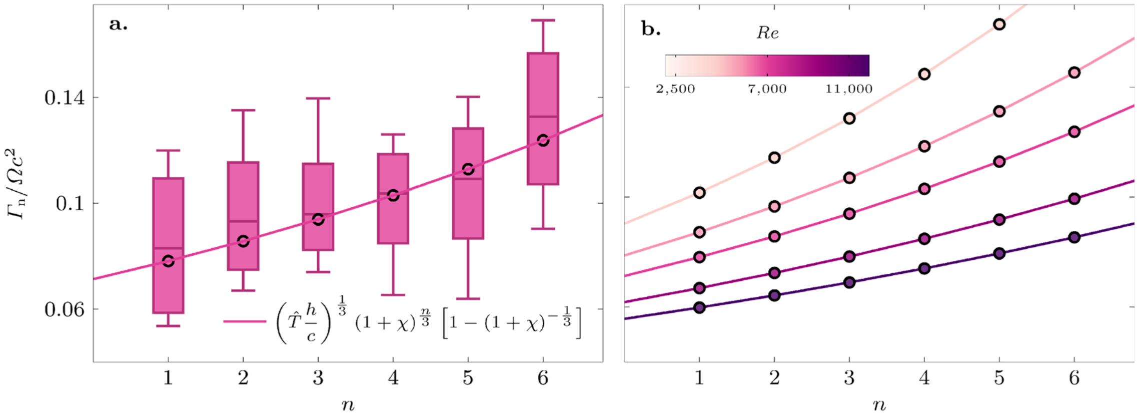

Fig. 8 **a** Comparison between circulation of all secondary vortices at Re = 5589 measured with the swirling strength criterion and predicted by Eq. (11). **b** Values of circulation computed with Eq. (11) for various Reynolds numbers

We can now use our previous results to estimate the evolution of the circulation of subsequently shed secondary vortices at different Reynolds numbers. The evolution of the total circulation is described by Eq. (4), with $K = 1.0$ independent of the plate dimensions. The timing of vortex shedding is given by Eq. (1), where α_0 depends on the plate dimensions $\alpha_0 = \hat{T}h/c$ with $\hat{T}$ the vortex formation number of the primary vortex, such that

$$\alpha_n(n) = \alpha_0(1+\chi)^n = \hat{T}\,\frac{h}{c}\,(1+\chi)^n \quad . \tag{9}$$

The circulation of the n^{th} secondary vortex is estimated by:

$$\frac{\Gamma_n}{\Omega c^2} = \frac{\Gamma(\alpha_n)}{\Omega c^2} - \frac{\Gamma(\alpha_{n-1})}{\Omega c^2} \tag{10}$$

$$= \left(\hat{T}\,\frac{h}{c}\right)^{\frac{1}{3}}(1+\chi)^{\frac{n}{3}}\left[1-(1+\chi)^{-\frac{1}{3}}\right] \tag{11}$$

For all experiments presented here, we found $\hat{T} = 10.9 \pm 0.6$. The parameter χ depends on the Reynolds number and decreases when the plate rotates faster according to Eq. (2).

The estimated circulation values determined using Eq. (11) are compared with the experimentally determined values in Fig. 8a for $\mathrm{Re} = 5589$. The secondary vortices are much smaller than the primary vortex and their resolution within the same region of interest is lower. Due to the limitations in the spatial resolution, there is substantial scatter in the data. To increase the statical significance we have combined here results from ten repetitions at $\mathrm{Re} = 5589$, combining the data for angular accelerations of $3000°/\mathrm{s}^2$ and $6000°/\mathrm{s}^2$. The timing of the shedding of the secondary vortices is easier to measure than their circulation. Still, the median measured values of the circulation of the secondary vortices are in good agreement with the estimated circulation computed with Eq. (11). Both confirm the increase in circulation with increasing order number.

4 Conclusions

The growth and timing of primary and secondary vortices generated by a rotating rectangular flat plate was investigated experimentally. Particular focus was directed towards the identification and prediction of the limit strength and formation number of primary and secondary vortices.

The total non-dimensional positive circulation generated at the tip of the rotation plate increases with $\alpha^{1/3}$ regardless of the geometry or the rotational speed of the plate. Initially, all circulation accumulates into the primary vortex which separates at $\alpha = \alpha_0$. The angle α_0 varies when the dimensions of the plate change. A constant vortex formation number or non-dimensional time delay $\hat{T} = \alpha_0 h/c = 10.9 \pm 0.6$ was found for all experiments presented.

The maximum non-dimensional limit value of the primary vortex circulation matches the total non-dimensional circulation at $\alpha = \alpha_0$ and can be estimated using inviscid theory. The non-dimensional primary vortex strength is independent of the rotational velocity based Reynolds number but varies depending on the plate's dimensions. The use of thicker plates leads to the formation of primary vortices that separate at higher values of α and reach higher non-dimensional limit circulation values. The use of longer plates leads to the formation of primary vortices that separate at lower values of α and reach lower non-dimensional limit circulation values.

The separation of the primary vortex is followed by the discrete release of secondary vortices for the tested range of Reynolds numbers from 2790 to 11170. The secondary vortices are considerably smaller in size and strength than the primary vortex. The non-dimensional strength of the secondary vortices is smaller than 20% of the primary vortex for all configurations tested. The non-dimensional strength of the secondary vortices is not constant but increases the more secondary vortices have been previously released and decreases with increasing Reynolds number. We proposed empirical predictions of the timing of shedding of subsequent secondary vortices as a function of the shedding order and Reynolds number. Combined with the experimentally determined constant primary vortex formation number of $\hat{T} = \alpha_0 h/c = 10.9 \pm 0.6$, we presented predictions of the strength of secondary vortices for a range of rotating plate motions that agree with the experimental observations.

Further measurements with more complex geometries and arbitrary motions are necessary to determine the range of validity and necessary adaptation of the proposed empirical model.

Appendix A Sensitivity analysis of the location and size of the average tip swirling strength probing region

The local average swirling strength $\overline{\lambda}_{tip}$ reaches a local maximum value when most of the vortex fills the selected rectangular region. We performed a variational analysis to select the most suitable position and dimension of the rectangular region which is discussed here.

The trajectories of the secondary vortices follow the modified Kaden's spiral introduced in Francescangeli and Mulleners (2021). Therefore, we decided to place a rectangular probing region of $0.25c \times 0.15c$ (width x height) along the spiral at $0.24c$ above the tip. The height of the probing region was large enough to fully include secondary vortices

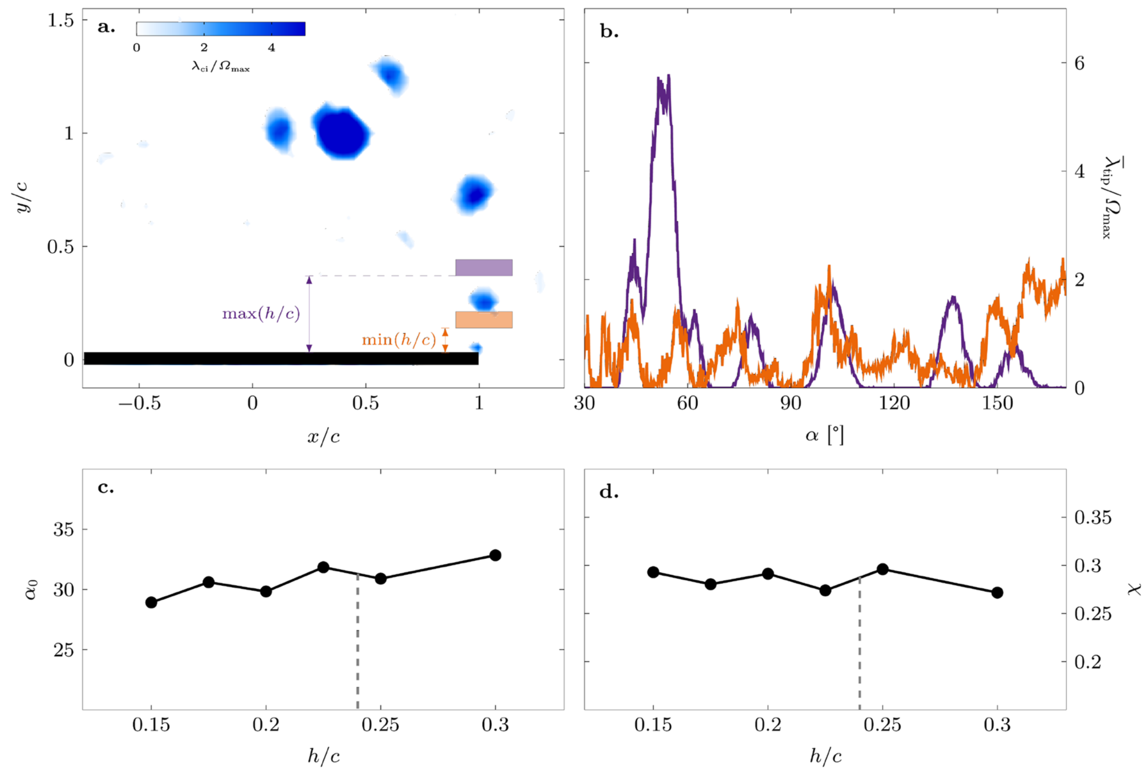

Fig. 9 **a** Snapshot of the scalar swirling strength field at $\alpha = 115°$ for *Re* =8380 including the locations of a the probing region at the maximal and minimal distance away from the tip ($y_p/c = 0.35$ and $y_p/c = 0.15$). **b** Temporal evolution of the average swirling strength $\overline{\lambda}_{tip}$ in the respective probing regions. Influence of vertical distance y_p/c between the probing region and the plate tip on the fitting coefficients **c** α_0 and **d** χ

but small enough not to include the swirling strength associated with the plate and the previous or following secondary vortices. The width of the region was as small as possible but sufficiently large to capture the secondary vortices even when small deviations to the predicted spiralling trajectory occurred.

This distance to the tip was the result of a compromise. If the distance between the probing region and the tip of the plate is larger than $0.35c$, the first two secondary vortices are not clearly distinguishable. The peak that corresponds to the presence of the primary vortex cannot be distinguished from the smaller peaks that correspond to the presence of the first two secondary vortices (Fig. 9a). If the probing region is too close to the tip of the plate, with the base at a distance lower than $0.12c$ from the tip, the signal is too noisy due to the presence of the bound vorticity accumulation at the tip (Fig. 9b).

We gradually moved the probing region in the range $0.15c < y_p < 0.35c$ and computed α_0 and χ at each location, to evaluate the influence of our choice. The coefficients α_0 and χ are the empirical fitting coefficients that predict the timing of the vortex shedding given by Eq. (1). When we move the probing region further away from the tip from 0.15 to 0.35 c, a delay in the identification of the vortices is introduced and the values of α_0 increase slightly from 29.9° to 32.8°. A correction to compensate for the delay could be applied but requires an estimation of the vortex speed between the moment of separation and the moment the vortex passes through the probing region and would introduce another empirical parameter. As the variations are relatively small compared to the overall fluctuations between runs in identifying α_0, we have not applied such a correction here. The influence of the location of the probing region on χ is not significant. The dashed line in Fig. 9e, f marks the location of the probing region used for the bulk of the results, which corresponds to the most robust choice for our test cases.

Appendix B Variation of α_0 and χ with Reynolds number

To facilitate readers to compare their results with those presented in this paper, we present in table 1 the empirical fitting coefficients α_0 and χ of Eq. (1) that predicts the timing of the vortex shedding. The same data is visually presented in Fig. 3.

Table 1 Values of α_0 and χ determined by fitting Eq. (1) to the experimentally determined timings of subsequent vortex shedding from the plate tip at different Reynolds numbers

Re	Min(α_0)	Median(α_0)	Max(α_0)	Min(χ)	Median(χ)	Max(χ)
2792	30.1	31.9°	33.6°	0.39	0.40	0.42
4189	30.7	31.2°	31.3°	0.35	0.38	0.39
5585	30.5°	32.2°	33.7°	0.29	0.31	0.33
8377	27.7°	30.4°	32.0°	0.25	0.27	0.29
11170	27.6°	30.4°	33.4°	0.21	0.24	0.26

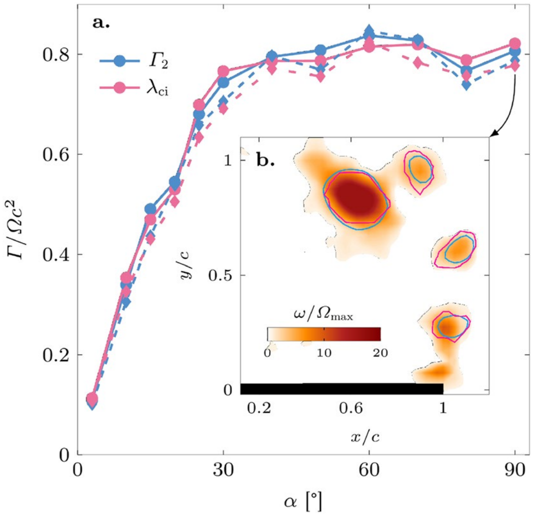

Fig. 10 **a** Comparison between dimensionless circulation of the primary vortex as a function of α, computed with the swirling strength and Γ_2 criteria. Continuous lines and dots represent circulation computed by integrating vorticity inside the contours. Dashed lines and diamond marks represent circulation computed by integrating the velocity around the contours. **b** Vorticity flow field at $\alpha = 90°$ for $Re = 8380$, overlapped with the swirling strength and Γ_2 contours

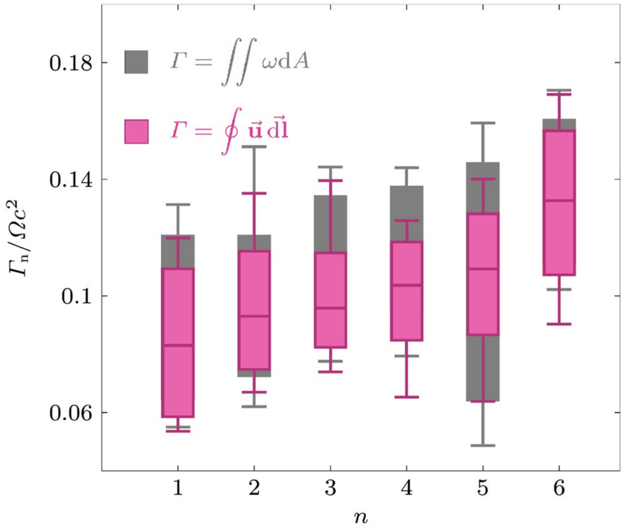

Fig. 11 Evolution of the circulation the secondary vortices at $\mathrm{Re} = 5589$ as a function of the shedding order n. The larger values correspond to the surface integration of the vorticity and the lower values to the line integration of the tangential velocity along the vortex boundaries identified using the swirling strength criterion

Appendix C Computation of the vortex circulation

To determine the circulation of the primary and secondary vortices shown in the results we have used the swirling strength criterion. Here, we compare the results using the swirling strength criterion (Zhou et al. 1999) with those obtained using the Γ_2 criterion (Graftieaux et al. 2001) to identify the vortex boundaries. The vortex circulation is determined by integrating either the vorticity within these boundaries or the velocity along the boundaries. An exemplary result of the comparison of the different methods is presented in Fig. 10a which shows the temporal evolution of the primary vortex circulation for the rotating reference plate at $Re = 8380$. The different colours refer to the swirling strength and the Γ_2 criterion to identify the vortex boundaries. The swirling strength criterion defines a vortex as compact region of negative swirling strength. We take the zero contour as the vortex boundary. The Γ_2 criterion considers the vortex core area as the region where $\Gamma_2 > 2/\pi$ and the $\Gamma_2 = 2/\pi$ contour is taken as the vortex boundary. A comparison between the different contours for the primary and secondary vortices at $\alpha = 90°$ is presented in Fig. 10b. The solid lines in Fig. 10a correspond to results obtained by a surface integral of the vorticity and the dashed lines correspond to results obtained by a line integral of the tangential velocity. Both identification techniques provide similar results and discrepancies between the various methods never exceed 5%.

For the larger primary vortex, little variation is observed between the surface integral of vorticity and the line integral of the velocity. For the smaller secondary vortices, the relative resolution of the velocity field measurements is lower and larger variations might be observed. In Fig. 11, we compare the evolution of the secondary vortices as a function of the shedding order using both integrations options for our reference plate at $\mathrm{Re} = 5589$. The vortex contours are identified using the swirling strength criterion which are slightly larger than the boundaries obtained from the Γ_2 criterion (Fig. 10b).

The area integrals of the vorticity yield slightly higher values of the circulation for all secondary vortices with larger variations between runs (grey box plots in Fig. 10). The larger variations are due to larger uncertainties that can occur when computing the velocity gradients for the vorticity. The line integrals of the velocity are less affected by outliers in the velocity field measurements and yield slightly lower values than the surface integrals. Overall, there is still a good agreement between both integration methods and both reveal the same increase of the circulation with increasing order of shedding.

Author contributions DF: Conceptualisation, Investigation, Writing—Original Draft, Visualisation KM: Conceptualisation, Writing—Review and Editing, Visualisation, Supervision.

Funding Open access funding provided by EPFL Lausanne.

Availability of data and materials Data will be made available upon reasonable request.

Declarations

Conflict of interest The authors declare no competing interests.

Ethical approval Not applicable.

References

Bloor MS (1964) The transition to turbulence in the wake of a circular cylinder. J Fluid Mech 19(02):290. https://doi.org/10.1017/S0022112064000726

Dabiri JO (2009) Optimal vortex formation as a unifying principle in biological propulsion. Ann Rev Fluid Mech 41(1):17–33. https://doi.org/10.1146/annurev.fluid.010908.165232

Dabiri JO, Gharib M (2005) Starting flow through nozzles with temporally variable exit diameter. J Fluid Mech 538:111–136. https://doi.org/10.1017/S002211200500515X

de Guyon G, Mulleners K (2021) Scaling of the translational velocity of vortex rings behind conical objects. Phys Rev Fluids 6(2):024701. https://doi.org/10.1103/PhysRevFluids.6.024701

de Guyon G, Mulleners K (2022) Estimating the non-dimensional energy of vortex rings by modelling their roll-up. J Fluid Mech 940:R2. https://doi.org/10.1017/jfm.2022.275

Eldredge JD, Jones AR (2018) Leading-Edge Vortices: Mechanics and Modeling. Annual Review of Fluid Mechanics 51(1):010518–040334. https://doi.org/10.1146/annurev-fluid-010518-040334

Fernando JN, Rival DE (2016) On vortex evolution in the wake of axisymmetric and non-axisymmetric low-aspect-ratio accelerating plates. Phys Fluids 28(1):017102. https://doi.org/10.1063/1.4938744

Francescangeli D, Mulleners K (2021) Discrete shedding of secondary vortices along a modified Kaden spiral. J Fluid Mech, 917. https://doi.org/10.1017/jfm.2021.259

Gao L, Yu SCM (2010) A model for the pinch-off process of the leading vortex ring in a starting jet. J Fluid Mech 656:205–222. https://doi.org/10.1017/S0022112010001138

Gehlert P, Babinsky H (2021) Boundary layer vortex sheet evolution around an accelerating and rotating cylinder. J Fluid Mech 915:A50. https://doi.org/10.1017/jfm.2021.121

Gehlert P, Andreu-Angulo I, Babinsky H (2023) Vortex force decomposition—forces associated with individual elements of a vorticity field. Submitted to Exp Fluids PREPRINT available at Research Square [https://doi.org/10.21203/rs.3.rs-2431774/v1]. https://doi.org/10.21203/rs.3.rs-2431774/v1

Gharib M, Rambod E, Shariff K (1998) A universal time scale for vortex ring formation. J Fluid Mech 360:121–140. https://doi.org/10.1017/S0022112097008410

Glezer A (1988) The formation of vortex rings. Phys Fluids 31(12):3532. https://doi.org/10.1063/1.866920

Graftieaux L, Michard M, Grosjean N (2001) Combining PIV, POD and vortex identification algorithms for the study of unsteady turbulent swirling flows. Measure Sci Technol 12(9):1422–1429. https://doi.org/10.1088/0957-0233/12/9/307

Greenblatt D, Williams DR (2021) Flow Control for Unmanned Air Vehicles. Ann Rev Fluid Mech 54(1):1–30. https://doi.org/10.1146/annurev-fluid-032221-105053

Grift EJ, Vijayaragavan NB, Tummers MJ et al (2019) Drag force on an accelerating submerged plate. J Fluid Mech 866:369–398. https://doi.org/10.1017/jfm.2019.102

Haller G (2001) Distinguished material surfaces and coherent structures in three-dimensional fluid flows. Phys D Nonlinear Phenomena 149(4):248–277. https://doi.org/10.1016/S0167-2789(00)00199-8

Haller G (2015) Lagrangian coherent structures. Ann Rev Fluid Mech 47(1):137–162. https://doi.org/10.1146/annurev-fluid-010313-141322

Huang Y, Green MA (2015) Detection and tracking of vortex phenomena using Lagrangian coherent structures. Exp Fluids 56(7). https://doi.org/10.1007/s00348-015-2001-z

Jones AR, Cetiner O, Smith MJ (2021) Physics and modeling of large flow disturbances: discrete gust encounters for modern air vehicles. Ann Rev Fluid Mech 54(1):1–25. https://doi.org/10.1146/annurev-fluid-031621-085520

Krishna S, Green MA, Mulleners K (2018) Flowfield and force evolution for a symmetric hovering flat-plate wing. AIAA J 56(4):1360–1371. https://doi.org/10.2514/1.J056468

Krueger PS (2008) Circulation and trajectories of vortex rings formed from tube and orifice openings. Phys D Nonlinear Phenomena 237(14–17):2218–2222. https://doi.org/10.1016/j.physd.2008.01.004

Krueger PS, Gharib M (2003) The significance of vortex ring formation to the impulse and thrust of a starting jet. Phys Fluids 15(5):1271–1281. https://doi.org/10.1063/1.1564600

Krueger PS, Dabiri JO, Gharib M (2006) The formation number of vortex rings formed in uniform background co-flow. J Fluid Mech 556:147. https://doi.org/10.1017/S0022112006009347

Limbourg R, Nedic J (2021a) An extended model for orifice starting jets. Phys Fluids 33(6):067,109. https://doi.org/10.1063/5.0048813

Limbourg R, Nedic J (2021b) On the asymptotic matching procedure predicting the formation number. Phys Fluids 33(11):117,103. https://doi.org/10.1063/5.0070542

Limbourg R, Nedić J (2021) An extension to the universal time scale for vortex ring formation. J Fluid Mech 915. https://doi.org/10.1017/jfm.2021.141

Linden PF, Turner JS (2001) The formation of "optimal" vortex rings, and the efficiency of propulsion devices. J Fluid Mech 427:61–72

Luchini P, Tognaccini R (2002) The start-up vortex issuing from a semi-infinite flat plate. J Fluid Mech 455:175–193. https://doi.org/10.1017/S0022112001007340

Milano M, Gharib M (2005) Uncovering the physics of flapping flat plates with artificial evolution. J Fluid Mech 534:403–409. https://doi.org/10.1017/S0022112005004842

Mohseni K, Gharib M (1998) A model for universal time scale of vortex ring formation. Phys Fluids 10(10):2436–2438. https://doi.org/10.1063/1.869785

Mohseni K, Ran H, Colonius T (2001) Numerical experiments on vortex ring formation. J Fluid Mech 430:267–282. https://doi.org/10.1017/S0022112000003025

Morton BR (1984) The generation and decay of vorticity. Geophys Astrophys Fluid Dyn 28(3–4):277–308. https://doi.org/10.1080/03091928408230368

Muijres FT, Johansson LC, Barfield R et al (2008) Leading-edge vortex improves lift in slow-flying bats. Science 319(5867):1250–1253. https://doi.org/10.1126/science.1153019

Mulleners K, Raffel M (2012) The onset of dynamic stall revisited. Exp Fluids 52(3):779–793. https://doi.org/10.1007/s00348-011-1118-y

Nobach H, Bodenschatz E (2009) Limitations of accuracy in PIV due to individual variations of particle image intensities. Exp Fluids 47(1):27–38. https://doi.org/10.1007/s00348-009-0627-4

Onoue K, Breuer KS (2016) Vortex formation and shedding from a cyber-physical pitching plate. J Fluid Mech 793:229–247. https://doi.org/10.1017/jfm.2016.134

Paraz F, Schouveiler L, Eloy C (2016) Thrust generation by a heaving flexible foil: Resonance, nonlinearities, and optimality. Phys Fluids 28(1):011903. https://doi.org/10.1063/1.4939499

Prasad A, Williamson CHK (1997) The instability of the shear layer separating from a bluff body. J Fluid Mech 333:375–402. https://doi.org/10.1017/S0022112096004326

Pullin DI (1978) The large-scale structure of unsteady self-similar rolled-up vortex sheets. J Fluid Mech 88(3):401–430. https://doi.org/10.1017/S0022112078002189

Pullin DI (1979) Vortex ring formation at tube and orifice openings. Phys Fluids 22(3):401. https://doi.org/10.1063/1.862606

Pullin DI, Perry AE (1980) Some flow visualization experiments on the starting vortex. J Fluid Mech 97(2):239–255. https://doi.org/10.1017/S0022112080002546

Pullin DI, Sader JE (2021) On the starting vortex generated by a translating and rotating flat plate. J Fluid Mech 906. https://doi.org/10.1017/jfm.2020.762

Pullin DI, Wang ZJ (2004) Unsteady forces on an accelerating plate and application to hovering insect flight. J Fluid Mech 509:1–21. https://doi.org/10.1017/s0022112004008821 journals.cambridge.org/action/displayAbstract?fromPage=onlineaid=227695fileId=S0022112004008821

Raffel M, Willert CE, Scarano F, et al (2018) Particle image velocimetry. Springer International Publishing

Ringuette MJ, Milano M, Gharib M (2007) Role of the tip vortex in the force generation of low-aspect-ratio normal flat plates. J Fluid Mech 581:453–468. https://doi.org/10.1017/S0022112007005976

Rival DE, Kriegseis J, Schaub P, et al (2014) Characteristic length scales for vortex detachment on plunging profiles with varying leading-edge geometry. Exp Fluids 55(1). https://doi.org/10.1007/s00348-013-1660-x

Rockwood MP, Taira K, Green MA (2017) Detecting vortex formation and shedding in cylinder wakes using Lagrangian coherent structures. AIAA J 55(1):15–23. https://doi.org/10.2514/1.J055051

Rosi GA, Rival DE (2017) Entrainment and topology of accelerating shear layers. J Fluid Mech 811:37–50. https://doi.org/10.1017/jfm.2016.716

Saffman PG (1975) On the formation of vortex rings. Stud Appl Math 54(3):261–268. https://doi.org/10.1002/sapm1975543261

Sattari P, Rival DE, Martinuzzi RJ, et al (2012) Growth and separation of a start-up vortex from a two-dimensional shear layer. Phys Fluids 24(10):107102. https://doi.org/10.1063/1.4758793

Shariff K, Leonard A (1992) Vortex rings. Ann Rev Fluid Mech 24(235):279

Shusser M, Gharib M (2000) Energy and velocity of a forming vortex ring. Phys fluids 12(3):618. https://doi.org/10.1063/1.870268

Shusser M, Gharib M, Mohseni K (1999) A new model for inviscid vortex ring formation. In: 30th Fluid dynamics conference. https://doi.org/10.2514/6.1999-3805

Shusser M, Gharib M, Rosenfeld M et al (2002) On the effect of pipe boundary layer growth on the formation of a laminar vortex ring generated by a piston/cylinder arrangement. Theor Comput Fluid Dyn 15(5):303–316. https://doi.org/10.1007/s001620100051

Shusser M, Rosenfeld M, Dabiri JO, et al (2006) Effect of time-dependent piston velocity program on vortex ring formation in a piston/cylinder arrangement. Phys Fluids 18(3):033601. https://doi.org/10.1063/1.2188918

Thompson MC, Leweke T, Hourigan K (2020) Bluff bodies and wake-wall interactions. Ann Rev Fluid Mech 53(1):1–30. https://doi.org/10.1146/annurev-fluid-072220-123637

Triantafyllou MS, Triantafyllou GS, Yue DKP (2000) Hydrodynamics of fishlike swimming. Ann Rev Fluid Mech 32(1):33–53. https://doi.org/10.1146/annurev.fluid.32.1.33

Wei T, Smith CR (1986) Secondary vortices in the wake of circular cylinders. J Fluid Mech 169(1):513. https://doi.org/10.1017/S0022112086000733

Weigand A, Gharib M (1997) On the evolution of laminar vortex rings. Exp Fluids 22(6):447–457. https://doi.org/10.1007/s003480050071

Willert C, Stasicki B, Klinner J, et al (2010) Pulsed operation of high-power light emitting diodes for imaging flow velocimetry. Measure Sci Technol 21(7):075402. https://doi.org/10.1088/0957-0233/21/7/075402

Xu L, Nitsche M (2015) Start-up vortex flow past an accelerated flat plate. Phys Fluids 27(3):033602. https://doi.org/10.1063/1.4913981

Zhou J, Adrian RJ, Balachandar S et al (1999) Mechanisms for generating coherent packets of hairpin vortices in channel flow. J Fluid Mech 387:353–396. https://doi.org/10.1017/S002211209900467X